Chapter 5

PHONON TRANSMISSION COEFFICIENTS AT SOLID INTERFACES

Chapter 5 has been adapted from

(*1*) Chengyun Hua et al. "Fresnel transmission coefficients for thermal phonons at solid interfaces". In: *In review process* (2016).

5.1 Background

Transport across interfaces in heterogeneous media is a fundamental physical process that forms the basis for numerous widely used technologies. For example, the reflection and transmission of light at interfaces, as described by the Fresnel equations, enables wave-guiding with fiber-optics and anti-reflection coatings, among many other functionalities. Interfaces also play an essential role in phonon-mediated heat conduction in solids.(*129*, *130*) Material discontinuities lead to thermal phonon reflections that are manifested on a macroscopic scale as a thermal boundary resistance (TBR), also called Kapitza resistance, R_k, that relates the temperature drop at the interface to the heat flux flowing across it. TBR exists at the interface between any dissimilar materials due to differences in phonon states on each side of the interface.(*129*) Typical interfaces often possess defects or roughness which can lead to additional phonon reflections and hence higher TBR.

TBR plays an increasingly important role in devices, particularly as device sizes decrease below the intrinsic mean free paths (MFPs) of thermal phonons.(*130*) At sufficiently small length scales, TBR can dominate the total thermal resistance. For instance, the effective thermal conductivity of a superlattice can be orders of magnitude smaller than that of the constituent materials due to high TBR.(*113*, *131–133*) This physical effect has been used to realize thermoelectrics with high efficiency(*9*,

12) and dense solids with exceptionally low thermal conductivity(*134*). On the other hand, TBR can lead to significant thermal management problems(*101*, *135*, *136*) in applications such as LEDs(*137*, *138*) and high power electronics(*136*, *139*).

Numerous works over several decades have investigated the microscopic origin of TBR at solid-solid interfaces, starting with studies performed at low temperatures ($\sim$ 1 K), in which heat is carried predominantly by phonons with frequencies less than 1 THz.(*140*, *141*) At these low temperatures and for pristine, ordered interfaces, transmission coefficients can be obtained from continuum elastic theory in an analogy with Snell's law for light; this model is known as the acoustic mismatch model (AMM).(*142*, *143*) The AMM was shown to explain the experimentally measured values of TBR at various solid-solid interfaces.(*141*) At higher temperatures (above 1 K), heat transport across the interfaces was found to be sensitive to surface roughness. For the limit of completely diffuse scattering in which transmitted and reflected phonons cannot be distinguished, Swartz constructed the diffuse mismatch model (DMM).(*129*) Despite the success of these models at explaining TBR at low temperatures, they generally fail at temperatures larger than 40 K and are unable to account for the atomistic structure of the interface.

Recent works have focused on remedying these deficiencies. Optical methods enable the routine measurement of TBR over a wide range of temperatures for various metal-dielectric interfaces (*26–30*) as well as at interfaces with variable bonding strength. (*31*, *32*) Other works have examined the temperature dependence of the thermal conductivity(*62*) in nanocrystalline samples. Computational atomistic methods such as molecular dynamics(*144–152*) and atomistic Green's functions(*153–157*) have been extensively applied to obtain the transmission coefficients at interfaces with realistic atomic structure. These calculations generally predict the coefficients to decrease with increasing phonon frequency due to reflections of short wavelength phonons by atomistic roughness, a trend that is supported

by basic wave physics and indirectly by experiment.(*62*, *158*) Despite all of these works, however, an unambiguous determination of the transmission coefficients at an actual interface has not yet been reported.

Here, we report the first measurements of the thermal phonon transmission coefficients at a solid interface using a combination of experimental observations of quasiballistic transport as introduction in Chapter 4 and advances in ab-initio transport modeling based on the Boltzmann transport equation (BTE) that are presented in Chapter 3. Unlike prior works in which considerable ambiguity remained in the values of the coefficients, our approach places tight constraints on the allowed spectral transmission profile. Applying our approach in conjunction with transmission electron microscopy (TEM), we are able to directly link atomic structure to the spectral content of heat crossing the interface for the first time. Our approach demonstrates a general route to directly experimentally study the microscopic transport processes governing interfacial heat conduction.

5.2 TDTR with ab-initio phonon transport modeling

Our measurement is based on the TDTR experiment, an optical pump-probe technique that is used to characterize thermal properties on micron length scales. In this experiment, a femtosecond pulsed laser beam is split into a pump and a probe beam. The pump pulse train is modulated at a frequency from 1 to 15 MHz to enable lock-in detection, and is then used to impulsively heat a metal film coated on the sample. The transient temperature decay at the surface is detected as a change in optical reflectance by the probe beam.(*159*) Extracting thermal properties requires solving a simple inverse problem in which the measured data sets are related to the desired properties by a macroscopic transfer function based on a multilayer heat diffusion model.(*160*, *161*) The thermal properties, such as substrate thermal conductivity and metal-substrate interface conductance are varied until the data and simulation

match.

Although this approach is widely used, it has the drawback that the microscopic phonon properties are averaged into a single number, the interface conductance, resulting in minimal constraints on the allowed transmission coefficients. In this work, we instead aim to directly and unambiguously extract the transmission coefficients from TDTR data by replacing the macroscopic transfer function based on Fourier's law with a microscopic transfer function based on ab-initio phonon transport modeling. Mathematically, we write this problem as:

$$g = H(T_{12}(\omega)), \tag{5.1}$$

where $T_{12}(\omega)$ are the phonon frequency dependent transmission coefficients from layer 1, the metal transducer film, to layer 2, the substrate; H is the transfer function based on ab-initio phonon transport modeling; and g is the TDTR experimental data consisting of multiple transient data sets with different modulation frequencies. This equation represents an inverse problem for the transmission coefficients that can in principle be solved in an analogous manner to that employed for the macroscopic transfer function.

Although simple in principle, several challenges arise when trying to implement this strategy. First, it is essential that part of the non-equilibrium phonon distribution emerging from the interface propagate into the substrate ballistically. As illustrated in Fig. 5.1, when MFPs are much shorter than the characteristic length scale of the thermal gradient, information about the phonon distribution at the interface is lost due to scattering. On the other hand, if some phonons have sufficiently long MFPs, the non-equilibrium phonon distribution penetrates into the substrate and affects the resulting heat conduction, thereby providing direct information about the spectral content of heat crossing the interface. Fortunately, many experimental reports have demonstrated clear evidence of this quasiballistic heat transport regime

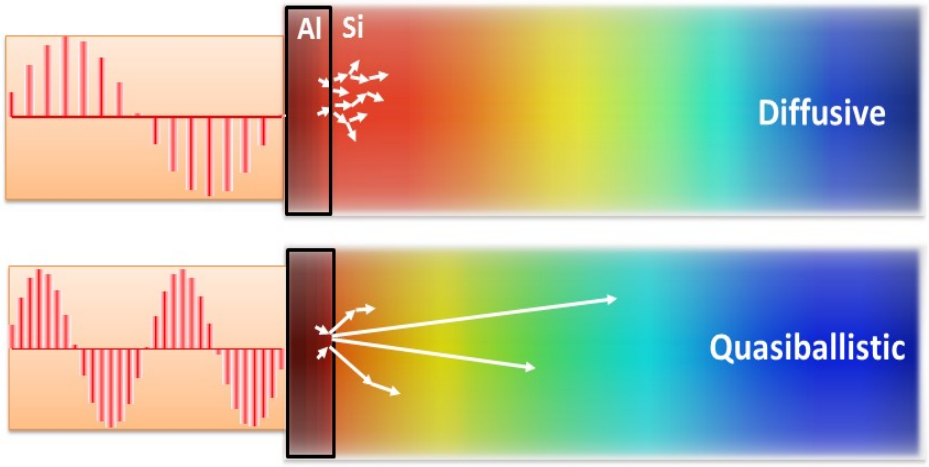

Figure 5.1: Schematic of the principle underlying the measurement of transmission coefficients. If the characteristic length scale of the thermal transport is much longer than the phonon MFPs, information about the interfacial distribution is lost due to strong scattering. If some MFPs are comparable to the thermal length scale, the non-equilibrium distribution at the interface propagates into the substrate where it can be detected.

in different material systems (*20*, *23*, *25*, *162–164*) including the transient thermal grating experiments discussed in Chapter 4. In this work, we interpret these effects as fundamentally originating from the non-equilibrium phonon distribution emerging from the interface.

Second, we must determine the microscopic transfer function that maps the transmission coefficients directly to the TDTR signal without any artificial fitting parameters. It is this step that has long impeded efforts to study interfaces due to the challenge of solving the BTE for the TDTR experiment. A number of simplified models(*79*, *126*, *164–168*) have been proposed to explain these observations. However, all of these models make various approximations that limit their predictive capability.

In this work, we overcome this challenge using two recent advances we reported for

rigorously solving the spectral BTE under the relaxation time approximation (RTA), with no additional simplifications, that yield a factor of 10^4 speedup compared to existing methods and allows the first ab-initio phonon transport modeling of TDTR free of artificial parameters or simplifications of the phonon dispersion. First, we have obtained an analytical solution of the spectral BTE in a semi-infinite substrate subject to an arbitrary heating profile.(*169*) Second, we have employed a series expansion method to efficiently solve the BTE in the thin transducer film.(*170*) In this work, these two solutions are combined using a spectral interface condition(*79*) that expresses the conservation of heat flux at each phonon frequency to yield the necessary microscopic transfer function $H(T_{12}(\omega))$.

5.3 Derivation of transfer function $H(T_{12}(\omega))$

We now describe the derivation of the transfer function $H(T_{12}(\omega))$ that maps transmission coefficients to the TDTR amplitude and phase data. Thermal transport in TDTR experiments, assuming only cross-plane heat conduction, is described by the one-dimensional (1D) spectral Boltzmann transport equation (BTE) under relaxation time approximation (RTA)(*22*),

$$\frac{\partial g_\omega}{\partial t} + \mu v_\omega \frac{\partial g_\omega}{\partial x} = -\frac{g_\omega + f_0(T_0) - f_0(T)}{\tau_\omega} + \frac{Q_\omega}{4\pi} \tag{5.2}$$

$$f_0(T) = \frac{1}{4\pi}\hbar\omega D(\omega) f_{BE}(T) \approx f_0(T_0) + \frac{1}{4\pi} C_\omega \Delta T, \tag{5.3}$$

where $g_\omega = \hbar\omega D(\omega)[f_\omega(x,t,\mu) - f_0(T_0)]$ is the deviational distribution function, $f_0 = f_0(x,t)$ is the equilibrium distribution function, $\mu = cos(\theta)$ is the directional cosine, v_ω is the phonon group velocity, τ_ω is the phonon relaxation time, and $Q_\omega(x,t)$ is the spectral volumetric heat generation. Assuming a small temperature rise, $\Delta T = T - T_0$, relative to a reference temperature, T_0, the equilibrium distribution is proportional to ΔT, as shown in Eq. (5.3). Here, $\hbar$ is the reduced Planck constant, ω is the phonon frequency, $D(\omega)$ is the phonon density of states, f_{BE} is the Bose-Einstein distribution, and $C_\omega = \hbar\omega D(\omega)\frac{\partial f_{BE}}{\partial T}$ is the mode specific

heat. The volumetric heat capacity is then given by $C = \int_0^{\omega_m} C_\omega d\omega$ and the Fourier thermal conductivity $k = \int_0^{\omega_m} k_\omega d\omega$, where $k_\omega = \frac{1}{3} C_\omega v_\omega \Lambda_\omega$ and $\Lambda_\omega = \tau_\omega v_\omega$ is the phonon MFP. To close the problem, energy conservation is used to relate g_ω to ΔT, given by

$$\int \int_0^{\omega_m} \left[\frac{g_\omega(x,t)}{\tau_\omega} - \frac{1}{4\pi} \frac{C_\omega}{\tau_\omega} \Delta T(x,t) \right] d\omega d\Omega = 0, \tag{5.4}$$

where Ω is the solid angle in spherical coordinates and ω_m is the cut-off frequency. Note that summation over phonon branches is implied without an explicit summation sign whenever an integration over phonon frequency or MFP is performed.

Before we solve Eq. (5.2), let us first briefly review the signal formation in TDTR. Since the thermal response given by the BTE is a linear time-invariant system, the output transient signal $Z(t)$ of TDTR can be represented in terms of frequency response solution through the following equation(*161*)

$$Z(t) = \sum_{n=-\infty}^{\infty} H(\omega_0 + n\omega_s) e^{in\omega_s t}, \tag{5.5}$$

where ω_0 is the reference angular frequency of the periodic heating, ω_s is the angular sampling frequency set by the repetition rate of the laser pulses, and $H(\eta)$ is surface temperature response subject to a periodic heating at frequency η. Therefore, to study the transient heat transport in TDTR, it is equivalent to solve the modulated heat conduction problem in the same geometry, a double-layer structure of a metal film on a substrate as shown in Fig. 5.2.

We now divide our discussion into three parts: transducer film, substrate, and interface. While the calculations for transducer film and substrate are treated using different techniques, the solutions in those two layers depend on each other through the appropriate interface conditions.

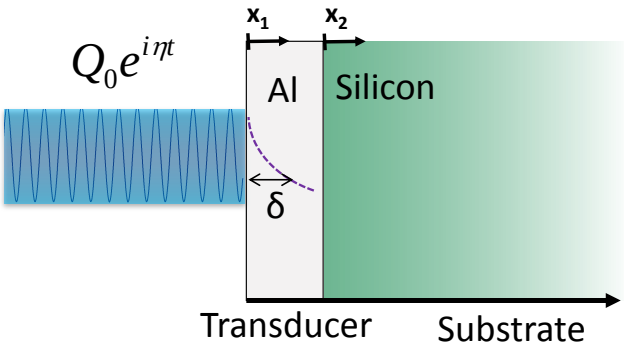

Figure 5.2: 2D schematic of the experimental configuration subject to a modulated heating source: a double layer structure of a transducer film on a substrate (sample). Q_0 is the amplitude of the heating source, η is angular modulation frequency, δ is the optical penetration depth of the heating source, and x is the cross-plane transport direction. x_1 and x_2 correspond to the coordinate systems used in transducer and substrate accordingly.

Transducer film

The metal thin film serves as an optical transducer that absorbs the incident optical energy, while also enabling the observation of temperature decay through the thermoreflectance coefficient. In our work, we neglect electrons and consider that heat is only carried by phonons in Al. This approximation is supported by prior works that found that the direct electron-phonon coupling transport mechanism is negligible for the materials considered here,(*26*, *171*, *172*) and thus the presence of electrons in our model is not necessary to accurately describe interfacial thermal transport for Al/Si interfaces. Moreover, in Section 5.11, we demonstrate the effects of electrons in Al are minimal to the TDTR signals.

Since the system is modulated at a given frequency η, we can assume that both $g_{1\omega}$ and ΔT_1 are of the form $e^{i\eta t}$. The volumetric heat generation in thin film is given by $Q_\omega = Q_\omega^0 e^{i\eta t} e^{-x_1/\delta}$, where the amplitude of heating source $Q_0 = \int_0^{\omega_m} Q_\omega^0 d\omega$. We also assume that phonons are specularly reflected at $x_1 = 0$, *i.e.* $\widetilde{g}_{1\omega}(x_1 =$

$0, \mu) = \widetilde{g}_{1\omega}(x_1 = 0, -\mu)$. Substituting $g_{1\omega} = \widetilde{g}_{1\omega}(x_1, \mu)e^{i\eta t}$, $\Delta T_1 = \Delta\widetilde{T}_1(x_1)e^{i\eta t}$ and the specular boundary condition at $x_1 = 0$ into Eq. (5.2) leads to a first-order ODE for $\widetilde{g}_{1\omega}(x_1, \mu)$, and its solution is given by

$$\begin{aligned}
\widetilde{g}^{+}_{1\omega}(x_1, \mu) &= B_\omega e^{-\frac{\gamma_{1\omega}}{\mu}(d+x_1)} + \int_0^d \frac{C_{1\omega}\Delta\widetilde{T}(x_1') + Q^0_\omega e^{-x/\delta}\tau_{1\omega}}{4\pi\Lambda_{1\omega}\mu} e^{\frac{\gamma_{1\omega}}{\mu}(x_1'+x_1)} dx_1' \\
&+ \int_0^{x_1} \frac{C_{1\omega}\Delta\widetilde{T}(x_1') + Q^0_\omega e^{-x/\delta}\tau_{1\omega}}{4\pi\Lambda_{1\omega}\mu} e^{\frac{\gamma_{1\omega}}{\mu}(x_1'-x_1)} dx_1' \ (\mu \in (0, 1]) \quad (5.6) \\
\widetilde{g}^{-}_{1\omega}(x_1, \mu) &= B_\omega e^{\frac{\gamma_{1\omega}}{\mu}(d-x_1)} \\
&- \int_x^d \frac{C_{1\omega}\Delta\widetilde{T}(x_1') + Q^0_\omega e^{-x/\delta}\tau_{1\omega}}{4\pi\Lambda_{1\omega}\mu} e^{\frac{\gamma_{1\omega}}{\mu}(x_1'-x_1)} dx_1' \ (\mu \in [-1, 0]), \quad (5.7)
\end{aligned}$$

where $\gamma_{1\omega} = (1 + i\eta\tau_{1\omega})/\Lambda_{1\omega}$, d is the film thickness, and B_ω are the unknown coefficients determined by the interface condition at $x_1 = d$. Here, $\widetilde{g}^{+}_{1\omega}(x_1, \mu)$ indicates the forward-going phonons and $\widetilde{g}^{-}_{1\omega}(x_1, \mu)$ the backward-going phonons.

To close the problem, we plug Eqs. (5.6) & (5.7) into Eq. (5.4) and obtained an integral equation for temperature as:

$$\Delta\widetilde{T}(\widehat{x}_1) - \int_0^1 \Delta\widetilde{T}(\widehat{x}_1')K(\widehat{x}_1', \widehat{x}_1)d\widehat{x}_1' = \int_0^{\omega_m} B_\omega F^1_\omega(\widehat{x}_1)d\omega + F^2(\widehat{x}_1), \quad (5.8)$$

where $\widehat{x}_1 = x_1/d$. The kernel function $K(\widehat{x}_1', \widehat{x})$ is given by

$$K(\widehat{x}_1', \widehat{x}_1) = \frac{1}{2\int_0^{\omega_m} \frac{C_{1\omega}}{\tau_{1\omega}} d\omega} \int_0^{\omega_m} \frac{C_{1\omega}}{\tau_{1\omega}\mathrm{Kn}_{1\omega}} \{E_1[\widehat{\gamma}_{1\omega}(\widehat{x}_1' + \widehat{x}_1)] + E_1[\widehat{\gamma}_{1\omega}|\widehat{x}_1' - \widehat{x}_1|]\} d\omega \quad (5.9)$$

and the two inhomogeneous functions are given by

$$\begin{aligned}
F^1_\omega(\widehat{x}_1) &= \frac{2\pi}{\int_0^{\omega_m} \frac{C_{1\omega}}{\tau_{1\omega}} d\omega} \frac{1}{\tau_{1\omega}} \{E_2[\widehat{\gamma}_{1\omega}(1 + \widehat{x}_1)] + E_2[\widehat{\gamma}_{1\omega}(1 - \widehat{x}_1)]\} \quad (5.10) \\
F^2(\widehat{x}_1) &= \frac{2\pi}{\int_0^{\omega_m} \frac{C_{1\omega}}{\tau_{1\omega}} d\omega} \int_0^1 \int_0^{\omega_m} \frac{Q^0_\omega e^{-\rho\widehat{x}_1'}}{\mathrm{Kn}_{1\omega}} \{E_1[\widehat{\gamma}_{1\omega}(\widehat{x}_1' + \widehat{x}_1)] + E_1[\widehat{\gamma}_{1\omega}|\widehat{x}_1' - \widehat{x}_1|]\} d\omega d\widehat{x}' \quad (5.11)
\end{aligned}$$

where $\mathrm{Kn}_{1\omega} = \Lambda_{1\omega}/d$ is the Knudsen number, $\widehat{\gamma}_{1\omega} = \frac{1+i\eta\tau_{1\omega}}{\mathrm{Kn}_{1\omega}}$, and $E_n(x)$ is the exponential integral given by(*21*):

$$E_n(x) = \int_0^1 \mu^{n-2} e^{-\frac{x}{\mu}} d\mu. \quad (5.12)$$

We apply the spectral method introduced in Section 3.3 to efficiently solve Eq. (5.8). Briefly, the functions in Eq. (5.8) can be expanded as a finite cosine series, such as

$$\Delta\widetilde{T}_{1(N)}(\widehat{x_1}) \approx \sum_{n=0}^{N} t_n \cos(n\pi\widehat{x_1}) \tag{5.13}$$

and

$$\begin{aligned} K_{(N)}(\widehat{x},\widehat{x'}) = \frac{1}{4}k_{00} \quad &+ \quad \frac{1}{2}\sum_{m=1}^{N} k_{m0} cos(m\pi\widehat{x}) + \frac{1}{2}\sum_{n=1}^{N} k_{0n} cos(n\pi\widehat{x'}), \\ &+ \quad \sum_{m=1}^{N}\sum_{n=1}^{N} k_{mn} cos(m\pi\widehat{x}) cos(n\pi\widehat{x'}) \end{aligned} \tag{5.14}$$

where N is the truncated basis number, and t_n's and k_{nm}'s are the Fourier coefficient. Similarly, $F^1_\omega(\widehat{x_1})$ and $F^2(\widehat{x_1})$ are also expanded in term of cosines. Following the steps in the above reference, we can express the temperature as

$$\Delta\widetilde{T}_1(\widehat{x_1}) = [\underline{\underline{A}}^{-1}(\underline{\underline{f_1}}\,\underline{B} + \underline{f_2})]^T \underline{\phi(x)} \tag{5.15}$$

where the matrix $\underline{\underline{A}}$ contains elements $A_{00} = 1 - \frac{k_{00}}{4}$, $A_{0n} = -\frac{1}{2}k_{0n}$, $A_{n0} = -\frac{k_{n0}}{4}$, $A_{nn} = 1 - \frac{1}{2}k_{nn}$ and $A_{nm} = -\frac{1}{2}k_{nm}$ $(m \neq n \neq 0)$ and $\underline{B}$ is a N_ω column vector of the unknown coefficients B_ω, where N_ω is the number of discretization in phonon frequency. $\underline{\underline{f_1}}$ is a $N \times N_\omega$ matrix, consisting of the Fourier coefficients of $F^1_{\omega_i}(\widehat{x_1})$ evaluated at each phonon frequency ω_i and $\underline{f_2}$ is a N column vector, consisting of the Fourier coefficients of $F^2(\widehat{x_1})$.

Then, $\widetilde{g}^+_{1\omega}(x_1,\mu)$ and $\widetilde{g}^-_{1\omega}(x_1,\mu)$ can be expressed in terms of the unknown coefficients B_ω by plugging Eq. (5.15) into Eqs. (5.6) and (5.7).

Substrate

The substrate can be treated as a semi-infinite region subject to a surface heat flux. Therefore, the BTE for the substrate becomes

$$i\eta\widetilde{g}_{2\omega} + \mu v_{2\omega}\frac{\partial\widetilde{g}_{2\omega}}{\partial x_2} = -\frac{\widetilde{g}_{2\omega}}{\tau_{2\omega}} + \frac{C_{2\omega}}{4\pi\tau_{2\omega}}\Delta\widetilde{T}(x_2) + \frac{1}{2}P_\omega v_{2\omega}|\mu|\delta(x_2), \tag{5.16}$$

where the unknown coefficients P_ω's are determined through the interface conditions.

We then apply the Green's function method given in Section 3.2. The unknown distribution function in spatial frequency domain is then written as

$$\widetilde{g}_{2\omega}(\eta,\xi_2) = \frac{C_{2\omega}}{4\pi}\frac{\Delta\widetilde{T}_2(\eta,\xi_2) + \frac{1}{2}P_\omega\Lambda_{2\omega}|\mu|/C_{2\omega}}{1+i\eta\tau_{2\omega}+i\mu\xi_2\Lambda_{2\omega}}, \tag{5.17}$$

and the temperature profile

$$\Delta\widetilde{T}_2(\eta,\xi_2) = \frac{\int_0^{\omega_m} P_\omega v_{2\omega}\frac{1+i\eta\tau_{2\omega}}{(\Lambda_{2\omega}\xi_2)^2}\log\left[1+\left(\frac{\Lambda_{2\omega}\xi_2}{1+i\eta\tau_{2\omega}}\right)^2\right]d\omega}{\int_0^{\omega_m}\frac{C_{2\omega}}{2\pi\tau_{2\omega}}\left[1-\frac{1}{\Lambda_{2\omega}\xi_2}\tan^{-1}\left(\frac{\Lambda_\omega\xi_2}{1+i\eta\tau_{2\omega}}\right)\right]d\omega}, \tag{5.18}$$

where ξ_2 is the Fourier variable of x_2.

Again, to express $\widetilde{g}_{2\omega}$ only in terms of unknown coefficients P_ω, we simply plug Eq. (5.18) into Eq. (5.17).

Interface condition

The unknown coefficients in the solutions of transducer film and substrate are obtained by applying appropriate interface conditions. Here, we use the elastic transmission interface condition with mode conversion, closely following the work by Minnich *et al.*(*79*) Briefly, for a given mode i, the heat fluxes outgoing from the interface, $q^{i-}_{1\omega}$ and $q^{i+}_{2\omega}$, must be equal to the reflected and transmitted heat fluxes incident to the interface, $q^{i+}_{1\omega}$ and $q^{i-}_{2\omega}$. By assuming elastic and diffuse scattering, the transmission and reflection process for each phonon frequency is treated independently and the heat flux equality condition must be satisfied for each frequency and polarization.

The interface conditions are

$$\int_0^1 g_{2\omega}^{i+} v_{2\omega}^i \mu d\mu = \sum_j T_{12}^{ji}(\omega) \int_0^1 g_{1\omega}^{j+} v_{1\omega}^j \mu d\mu + \sum_j R_{21}^{ji}(\omega) \int_0^1 g_{2\omega}^{j-} v_{2\omega}^j \mu d\mu, \tag{5.19}$$

$$\int_0^1 g_{1\omega}^{i-} v_{1\omega}^i \mu d\mu = \sum_j T_{21}^{ji}(\omega) \int_0^1 g_{2\omega}^{j-} v_{2\omega}^j \mu d\mu + \sum_j R_{12}^{ji}(\omega) \int_0^1 g_{1\omega}^{j+} v_{1\omega}^j \mu d\mu, \tag{5.20}$$

where $T_{12}^{ji}(\omega)$ is the transmission coefficient of mode j at frequency ω from side 1 to side 2 as mode i, $R_{21}^{ji}(\omega)$ is the reflection coefficient of mode j at frequency ω from side 2 back into side 2 as mode i, and so on. $g_{1\omega}^{i\pm}$ from Sec. 5.3 and $g_{2\omega}^{i\pm}$ from Sec. 5.3 are evaluated at $x_1 = d$ and at $x_2 = 0$, respectively. Given the values of $T_{12}^{ij}(\omega)$, $R_{12}^{ij}(\omega)$, $T_{21}^{ij}(\omega)$ and $R_{21}^{ij}(\omega)$, the unknown coefficients P_ω and B_ω's are obtained by plugging Eqs. (5.6), (5.7), and (5.17) into Eqs. (5.19) and (5.20) and solving the linear system.

The next question is how $T_{12}^{ij}(\omega)$ is related to the other reflection and transmission coefficients. The reflection coefficients are related to the transmission coefficients by energy conservation given by

$$\sum_j T_{12}^{ij}(\omega) + R_{12}^{ij}(\omega) = 1, \tag{5.21}$$

and

$$\sum_j T_{21}^{ij}(\omega) + R_{21}^{ij}(\omega) = 1. \tag{5.22}$$

$T_{21}^{ji}(\omega)$ is related to $T_{12}^{ij}(\omega)$ through the principle of detailed balance, which requires that no net heat flux can transmit across the interface when both materials are at an equilibrium temperature T. Applying this condition to every phonon mode on each side of the interface for each polarization and frequency gives:

$$T_{12}^{ij}(\omega) C_{1\omega}^i v_{1\omega}^i = T_{21}^{ji}(\omega) C_{2\omega}^j v_{2\omega}^j. \tag{5.23}$$

Therefore, we need to specify $T_{12}^{ij}(\omega)$, $R_{12}^{ij}(\omega)$, and $R_{21}^{ij}(\omega)$.

Let us first consider a special case where no mode conversion is allowed ($T_{12}^{ij}(\omega)$, $T_{21}^{ij}(\omega)$, $R_{12}^{ij}(\omega)$, $R_{21}^{ij}(\omega) = 0$ for $i \neq j$). Then, the interface conditions become

$$\int_0^1 g_{2\omega}^{i+} v_{2\omega} \mu d\mu = T_{12}^{ii}(\omega) \int_0^1 g_{1\omega}^{i+} v_{1\omega}^{i} \mu d\mu + R_{21}^{ii}(\omega) \int_0^1 g_{2\omega}^{i-} v_{2\omega}^{i} \mu d\mu, \quad (5.24)$$

$$\int_0^1 g_{1\omega}^{i-} v_{1\omega} \mu d\mu = T_{21}^{ii}(\omega) \int_0^1 g_{2\omega}^{i-} v_{2\omega}^{i} \mu d\mu + R_{12}^{ii}(\omega) \int_0^1 g_{1\omega}^{i+} v_{1\omega}^{i} \mu d\mu, \quad (5.25)$$

and the detail balance becomes

$$T_{12}^{ii}(\omega) C_{1\omega}^{i} v_{1\omega}^{i} = T_{21}^{ii}(\omega) C_{2\omega}^{i} v_{2\omega}^{i}. \quad (5.26)$$

Therefore, once $T_{12}^{ii}(\omega)$ is specified, all the other transmission and reflection coefficients are determined. For now, we only consider this special case and neglect the mode conversion in our BTE simulations. In Section 5.11, we show that the mode specific transmission coefficients cannot be resolved by the TDTR measurements and the measurable quantity is $\sum_j T_{12}^{ij}(\omega)$ instead of individual transmission coefficients. For simplicity, we will use $T_{12}(\omega, p)$ rather than the summation. Note that the only inputs to our calculation are the phonon dispersions and lifetimes, calculated using density functional theory (DFT) with no adjustable parameters by Jesús Carrete and Natalio Mingo using ShengBTE(*88*) and Phonony(*173*) from interatomic force constants obtained with VASP.(*91–94*) The details about converting the ab-initio calculations to an equivalent isotropic dispersion to reduce computational cost can be found in Appendix C. For Aluminum, the dispersion is calculated using the harmonic interatomic force constants, which are generated using Density Functional Perturbation Theory (DFPT) implemented in the ab-initio simulation package Quantum Espresso. The details about calculating phonon lifetimes in Al are given in Appendex D.5. Fig. 5.3 plots the phonon density of states, group velocity, and relaxation times as a function of phonon frequency in both Al and Si for the three acoustic branches.

The only unknown parameters in this model are the spectral transmission coefficients $T_{12}(\omega)$. In this work, we use $T_{12}(\omega)$ as the fitting parameter rather than using

models like a gray model or DMM. The result of the BTE modeling can be written into a compact transfer function given as

$$g = H(T_{12}(\omega)), \tag{5.27}$$

where H is the microscopic transfer function based on BTE modeling, and g is the TDTR experimental data consisting of multiple transient data sets with different modulation frequencies. This microscopic transfer function maps the spectral transmission coefficients $T_{12}(\omega)$ into an observable quantity g. This equation can be solved as an inverse problem for the transmission coefficients. Therefore, we are able to interpret phonon transmission coefficients across an interface directly from the experiments without any artificial fitting parameters.

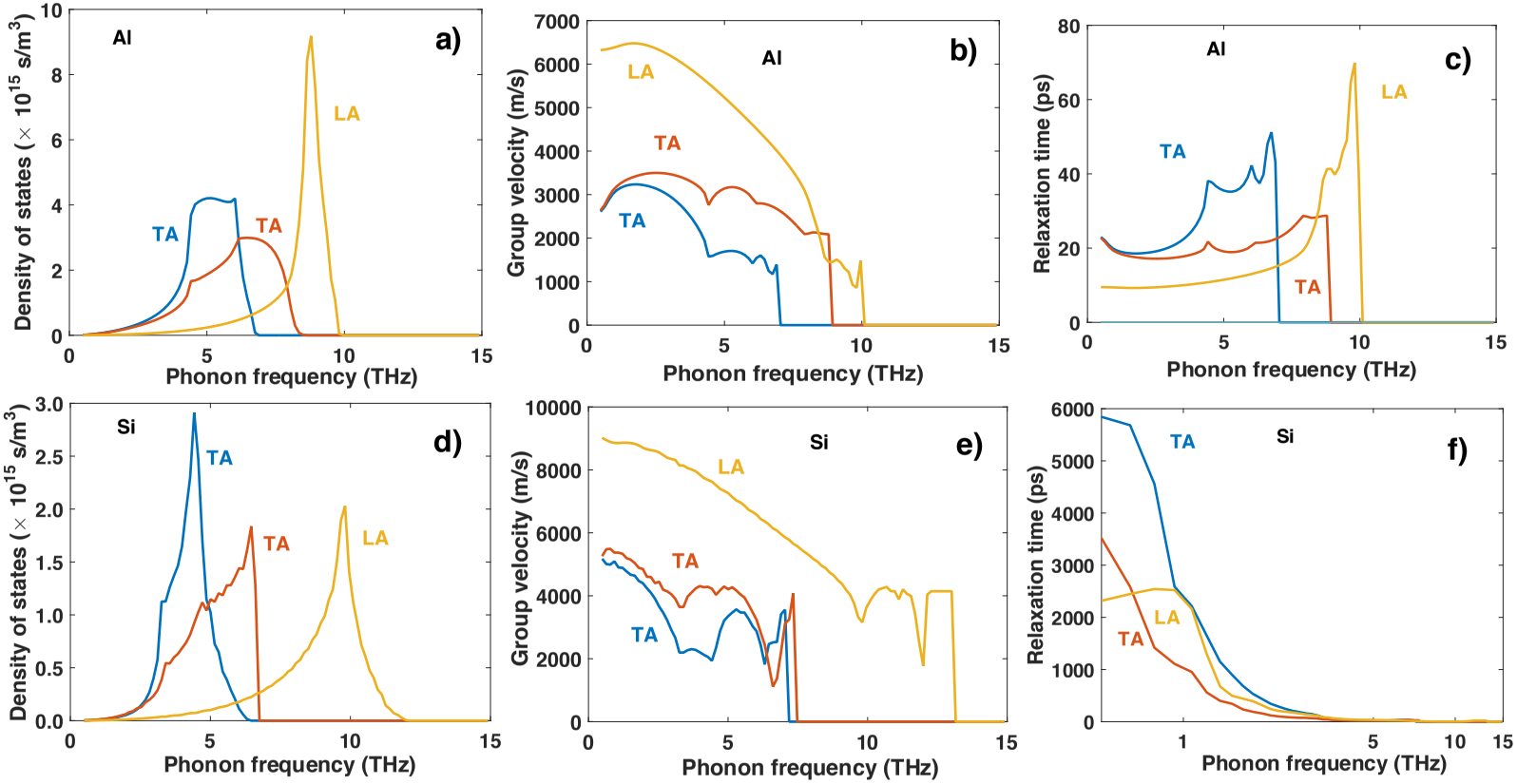

Figure 5.3: (a) Phonon density of states, (b) group velocity, and (c) relaxation times vesus phonon frequency for Al; (d) Phonon density of states, (e) group velocity, and (f) relaxation times versus phonon frequency for Silicon. Blue and red lines represent transverse acoustic modes, and yellow lines represent longitudinal acoustic modes.

5.4 Solution of inverse problem

The final challenge is to solve the inverse problem that identifies the transmission coefficients that best explain the observed data. From the BTE model, we obtain a surface temperature decay curve as a function of time just like the one measured in the experiments. For a given sample, the correct transmission coefficient profile as a function of phonon frequency will minimize the difference between the simulation curves and experimental TDTR traces at all modulation frequencies. By treating the transmission coefficients as fitting parameters, we avoid using the oversimplified models. To solve the inverse problem that identifies the transmission coefficients that best explain the observed data, we utilized particle swarm optimization (PSO) method to search for the optimal profile. The essential goal of PSO method is to minimize the objective function defined as

$$f = \alpha |g_{ab-initio}(T_{12}(\omega)) - g_{measured}| + (1-\alpha) \int \left(\frac{d^2 T_{12}}{d\omega^2} \right)^2 d\omega. \tag{5.28}$$

The first part of the equation evaluates the norm of the difference between the experimentally measured and BTE-simulated TDTR signals given a transmission profile profile $T_{12}(\omega)$. The second part of the equation evaluates the second derivative of the transmission coefficient profile, serving as the smoothness penalty function. Note that the smoothness of the profiles is the only constraint we impose in the objective function. The smoothing parameter α determines the relative importance of the second part to the first part. If $\alpha = 1$, then no smoothness constraint is imposed. Here, we use

$$\alpha = \frac{\int \left(\frac{d^2 T_{12}^0}{d\omega^2} \right)^2 d\omega}{|g_{ab-initio}(T_{12}^0(\omega)) - g_{measured}|}, \tag{5.29}$$

where $T_{12}^0(\omega)$ is the initial profile. The formula is chosen such that the first and second parts of the equation have the same order of magnitude.

To search for the optimal profile that minimizes the objective function, the PSO algorithm randomly initializes a collection of transmission coefficient profiles and

evolves them in steps throughout the phase space which contains all possible transmission coefficient profiles. At each step and for each profile, the algorithm evaluates the objective function defined as above. After this evaluation, the algorithm decides how each profile should evolve according to the current best profile. The profile evolves, then the algorithm reevaluates. The algorithm stops when the objective function reaches the desired value. The transmission coefficient profile that achieves the minimum value of the objective function is the optimal profile that explains the data.

However, since the inverse problem is ill-posed, a unique solution does not exist. We use Gibbs sampling to explore adjacent regions of the optimal transmission coefficient profile. We first randomly generated 1000 profiles by perturbing the optimal profile with a smooth function defined using the following formula

$$\delta = A[r_1 \cos(2\pi\omega/\omega_{max} r_2 + 2\pi r_3) + r_4 \sin(2\pi\omega/\omega_{max} r_5 + 2\pi r_6)], \tag{5.30}$$

where the amplitude of the perturbation A is 0.1, and r_1, r_2, r_3, r_4, r_5 and r_6 are random numbers between 0 to 1. We evaluated the objective function at all the perturbed profiles and recorded the values. Then, we started the Gibbs sampling process. At each iteration, we randomly drew a profile, a, from the stored population and compared the value of its corresponding objective function, f_n to the one from the previous step, f_{n-1} evaluated at profile b. If f_n is less than f_{n-1}, we accepted a and kept f_n. If not, a random number r was drawn and compared to $u = p/(1+p)$, where

$$p = \exp\left(\frac{f_n - f_{n-1}}{T_0}\right). \tag{5.31}$$

If r was smaller than u, then we accepted a and kept f_n. If not, we rejected a and updated f_n to be f_{n-1}. The system temperature, T_0, is chosen such that the stationary distribution is gradually changing. Here, T_0 is set to be the mean value of the objective functions of all the perturbed samples. We kept track of how many times each

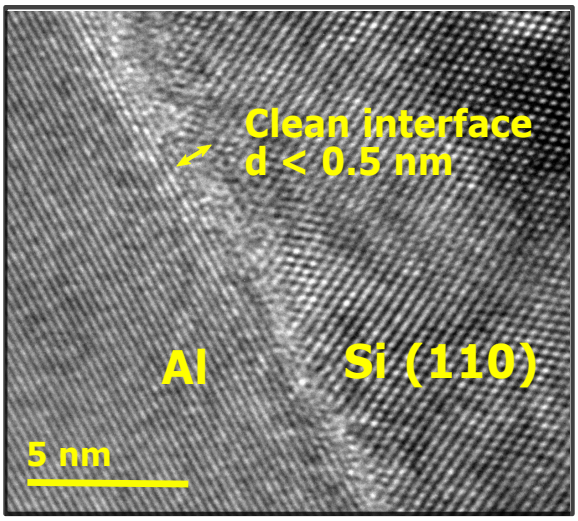

Figure 5.4: TEM image showing the clean interface of an Al/Si sample with the native oxide removed. The interface thickness is less than 0.5 nm.

profile was chosen at each iteration and generated a histogram of the occurrence frequency of each profile. We stopped the sampling process when the histogram became stationary. This occurrence frequency is also called the likelihood of the transmission coefficient profiles. The higher the value of a profile's likelihood is, the more likely the profile could fit the experimentally measured TDTR signals at different modulation frequencies. Thus by combining the PSO method with Gibbs sampling algorithm, we are able to determine the most likely transmission coefficients at the interface between Si and Al.

5.5 Measurements of phonon transmission coefficients

We demonstrate our transmission coefficient measurements on an Al film on Si substrate with the native oxide removed by Hydrofluoric acid prior to Al deposition, yielding a clean interface. The TEM image in Fig. 5.4 shows the interface thickness is less than 0.5 nm. The amplitude and phase of signals from the lock-in amplifier at different modulation frequencies are given in Fig. 5.5. For reference, solving the usual inverse problem with the macroscopic transfer function on this

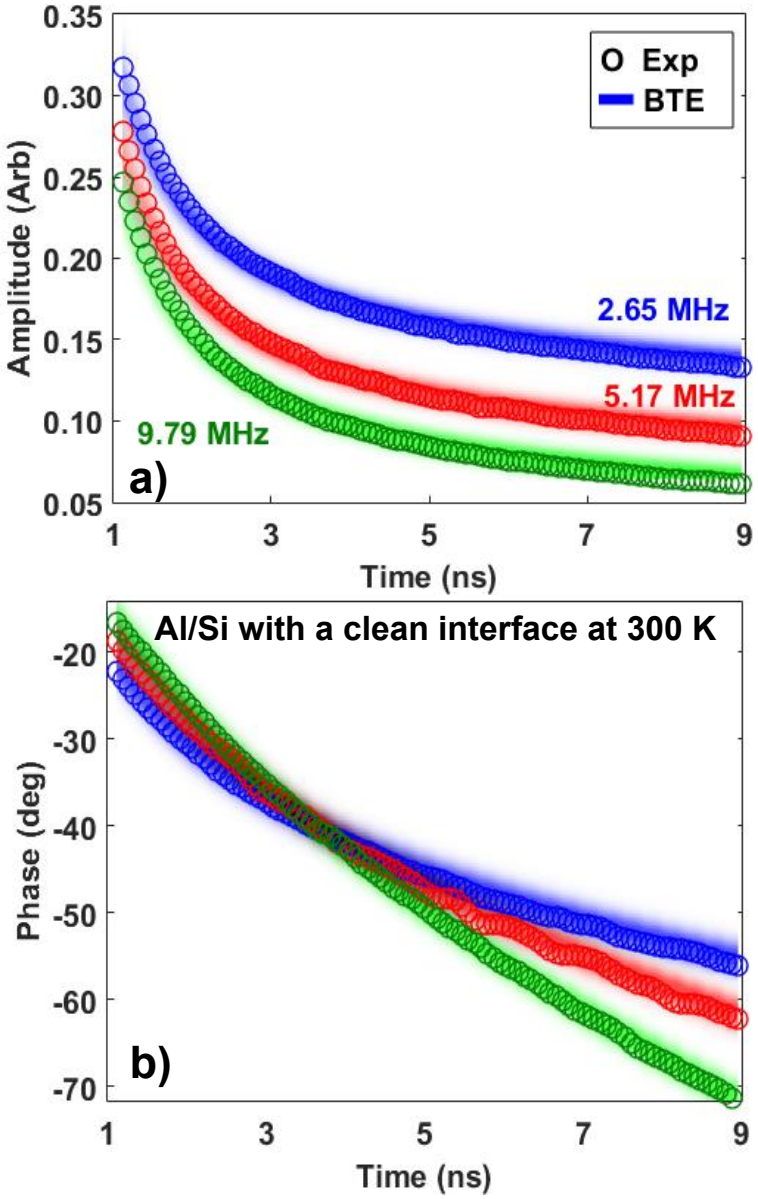

Figure 5.5: Experimental TDTR data (symbols) on this sample at $T = 300$ K for modulation frequencies $f = 2.68$, 5.51 and 9.79 MHz along with the (a) amplitude and (b) phase fit to the data from the BTE simulations (shaded regions), demonstrating excellent agreement between simulation and experiment. The shaded stripes denoted BTE simulations correspond to the likelihood of the measured transmission coefficients possessing a certain value as plotted in Fig. 5.6.

data set yields $G \approx 280$ MW/m^2-K and $k \approx 140$ W/m-K, in good agreement with prior works and literature values for the thermal conductivity of Si.(*20*, *158*) Although the good agreement is often taken as evidence that the macroscopic transfer function is valid for Si, this conclusion is incompatible with several independent ab-initio calculations that clearly show that heat is carried by phonons with MFPs exceeding the thermal penetration depth of TDTR.(*174*, *175*) This prediction has recently been experimentally confirmed by Cuffe *et al* using thermal measurements on variable thickness silicon membranes.(*176*) This fact implies that quasiballistic transport should be readily observable in a typical TDTR experiment on Si, despite the seemingly correct thermal properties measured. This apparent contradiction is resolved by observing that the signal measured in TDTR strongly depends on the spectral profile of the transmission coefficients in the quasiballistic regime, thereby providing the sensitivity necessary to solve the inverse problem given in Eq. 5.27.

We represent the transmission coefficient as a probability density plot, with the color intensity indicating the likelihood that a single transmission coefficient curve passing through a particular point at a given phonon frequency is able to simultaneously explain all of the data in Fig. 5.5, without any other adjustable parameters. The result is shown in Fig. 5.6(a). The figure shows that the transmission coefficient from Si to Al for longitudinal phonons, $T_{Si\rightarrow Al}(\omega)$, starts at unity, its maximum possible value, and decreases steadily to near zero for high phonon frequencies ($\sim$ 10 THz). The transmission coefficient profiles for the other polarizations have similar shapes, and so throughout the paper we plot only the longitudinal transmission coefficients for simplicity. The transmission coefficients from Al to Si, $T_{Al\rightarrow Si}(\omega)$ are calculated by satisfying the principle of detailed balance; the relationship between $T_{Si\rightarrow Al}(\omega)$ and $T_{Al\rightarrow Si}(\omega)$ reflects the differences in density of states and group velocity between the two materials. The transmission coefficients for each side of the interface and for the other polarizations are given in Appendix D.2.

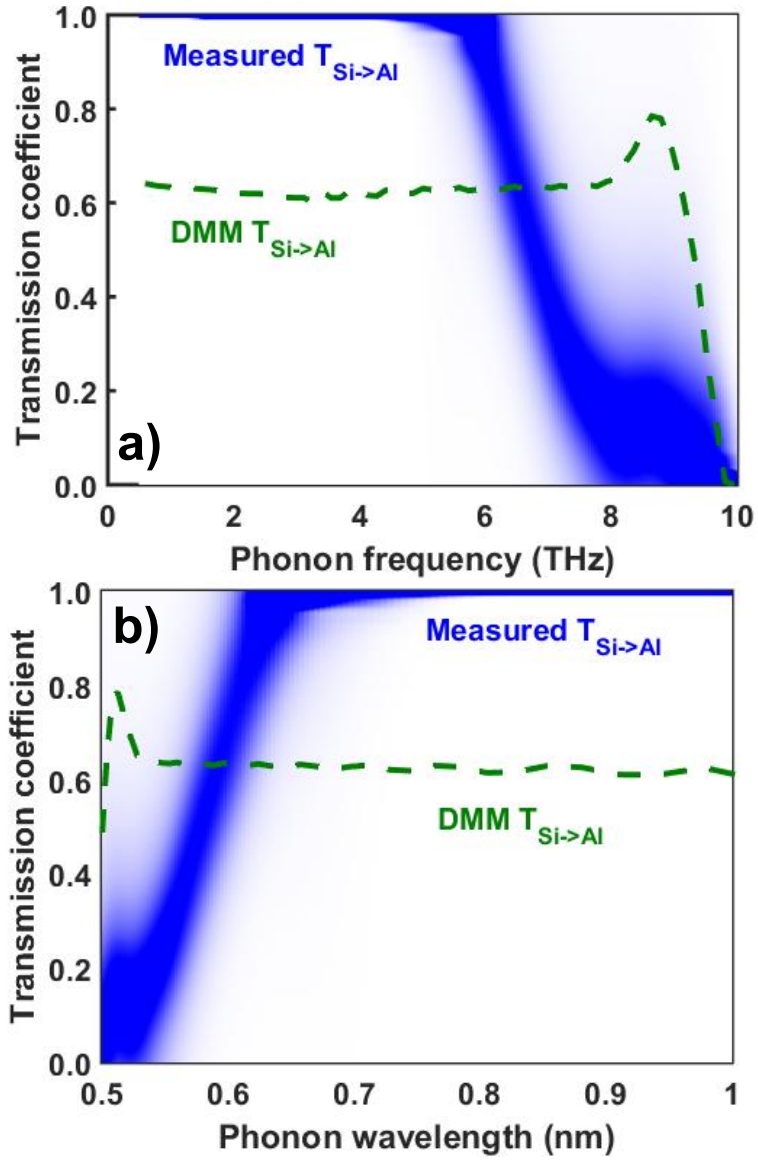

Figure 5.6: Transmission coefficients of longitudinal phonons $T_{Si\rightarrow Al}(\omega)$ (blue shaded region) versus (a) phonon frequency and (b) phonon wavelength, along with the DMM transmission coefficient profile (green dashed line) that gives the same interface conductance as the measured $T_{Si\rightarrow Al}(\omega)$. The intensity of the shaded region corresponds to the likelihood that the transmission coefficient possesses a given value.

Our measured transmission coefficient profile thus indicates that phonons with frequencies less than 4 THz are transmitted to the maximum extent allowed by the principle of detailed balance, while phonons with frequencies larger than 8 THz are nearly completely reflected at the interface. We now examine this result in context with the common models for transmission coefficients. The AMM is often cited as an appropriate model for transmission coefficients at sufficiently low phonon frequencies. At low phonon frequency ($<$ 1 THz), we find that at normal incidence, the transmission coefficients given by AMM is consistent with the measured value. However, the experimental work of Swartz and Pohl(*129*) clearly indicates that even for expitaxial interfaces the validity of the AMM is limited to phonons with frequencies in the hundreds of GHz that carry a small fraction of the heat at room temperature. Therefore, the AMM is not applicable for a wide spectrum of phonons studied here. For short wavelength phonons, the DMM would be expected to apply. At the highest phonon frequencies (shortest wavelengths), the DMM correctly predicts the trend of the measured transmission coefficients tending to zero. However, for most of the phonon spectrum, the DMM is inconsistent with our measurement as discussed in the following section.

5.6 Comparison of conventional models

In this section we provide additional evidence for the inadequacy of conventional models to explain our measurements. We consider two models: the gray model in which the transmission coefficient is a constant, independent of phonon frequency, and the diffuse mismatch model (DMM). The DMM is only determined by the phonon properties of the materials, such as density of states and phonon group velocity. Figs. 5.7(a) & (b) show the transmission coefficients from both sides of the interface using the DMM. The constant transmissivity value is chosen to yield an interface conductance G = 284 MW/m^2-K using the formula of Ref. (*79*). The

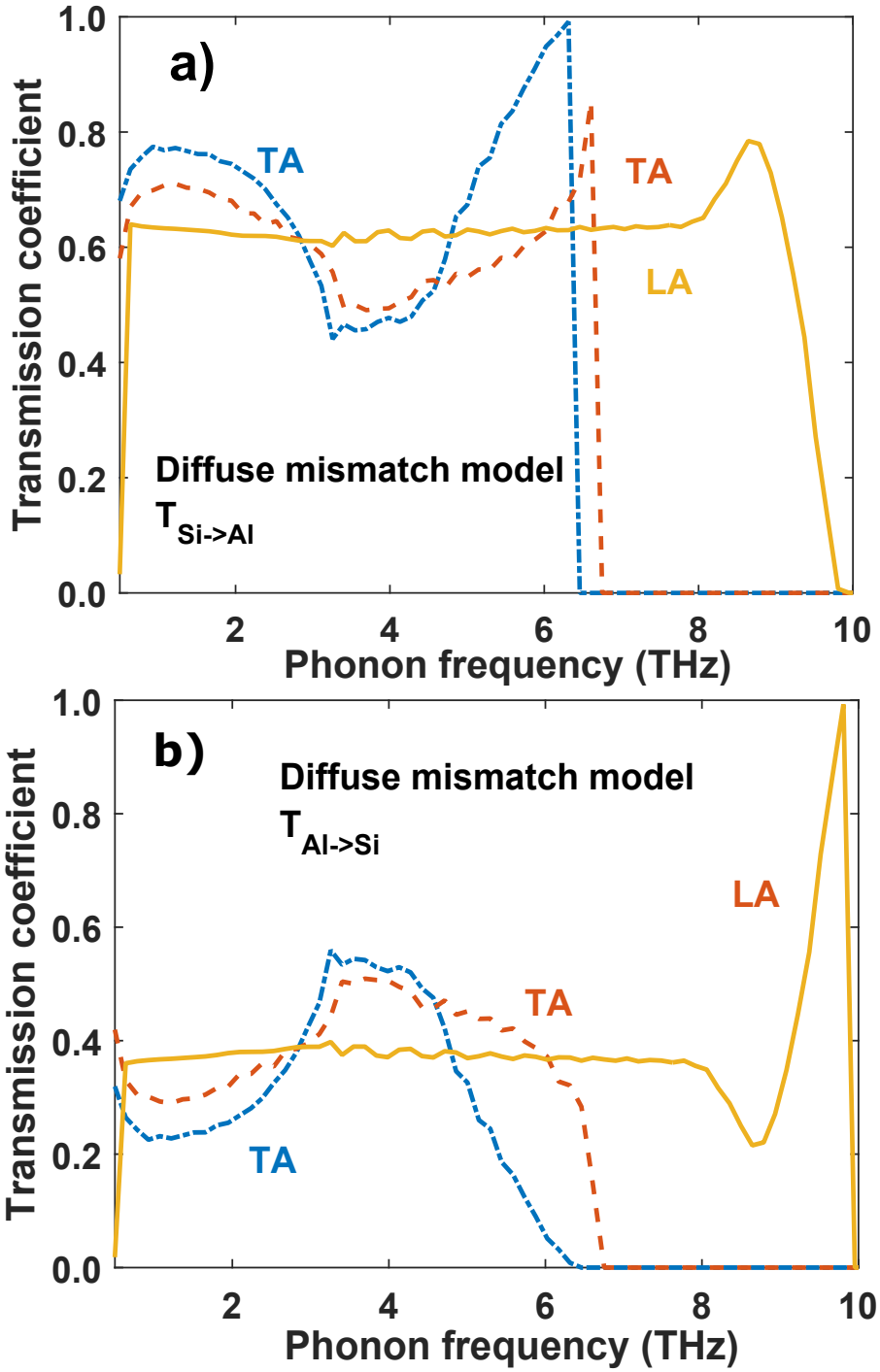

Figure 5.7: Transmission coefficients predicted by diffuse mismatch model (DMM) for each polarization (a) from Si to Al and (b) from Al to Si.

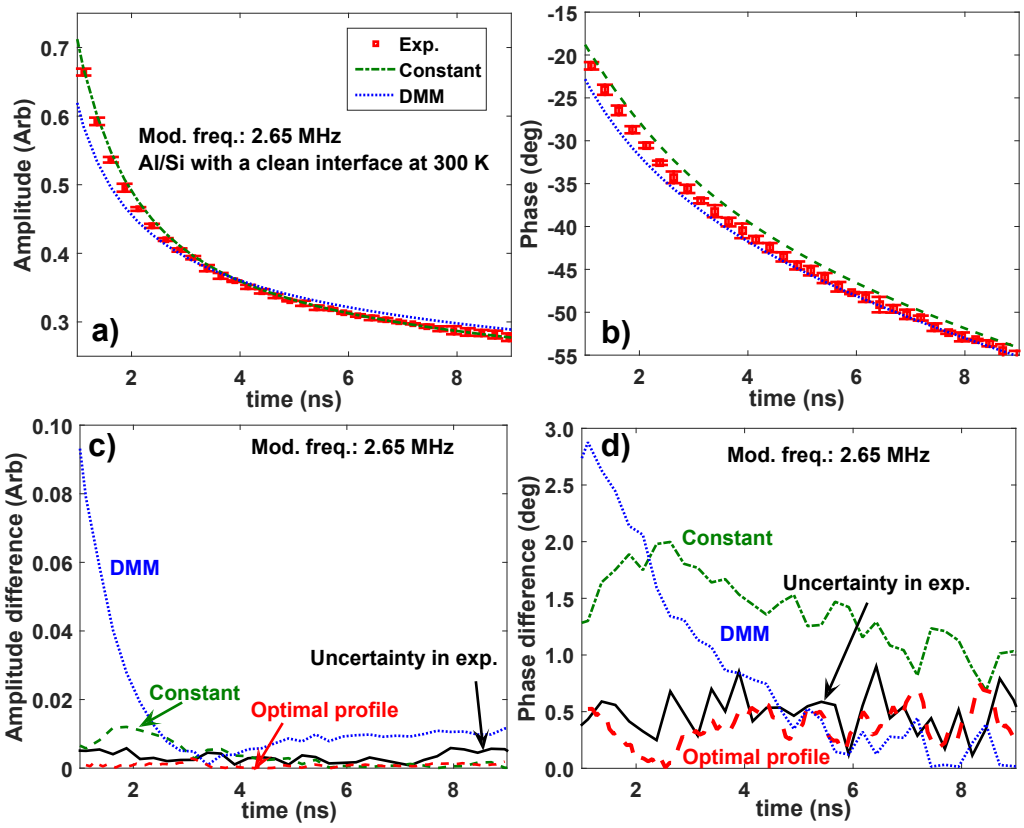

Figure 5.8: Experimental TDTR data (symbols) on Al/Si with a clean interface at 300 K for modulation frequency $f = 2.65$ MHz along with the (a) amplitude and (b) phase compared to the data from the BTE simulations using constant $T_{Si \to Al}$ (dash-dotted lines) and DMM (dotted lines). (c) Amplitude and (d) phase difference between averaged experimental data and the BTE simulations using constant $T_{Si \to Al}$ (dash-dotted lines), DMM (dotted lines), and the optimal profile in Fig. 2 of the main text (dashed lines). The solid line indicates the uncertainty in experiments.

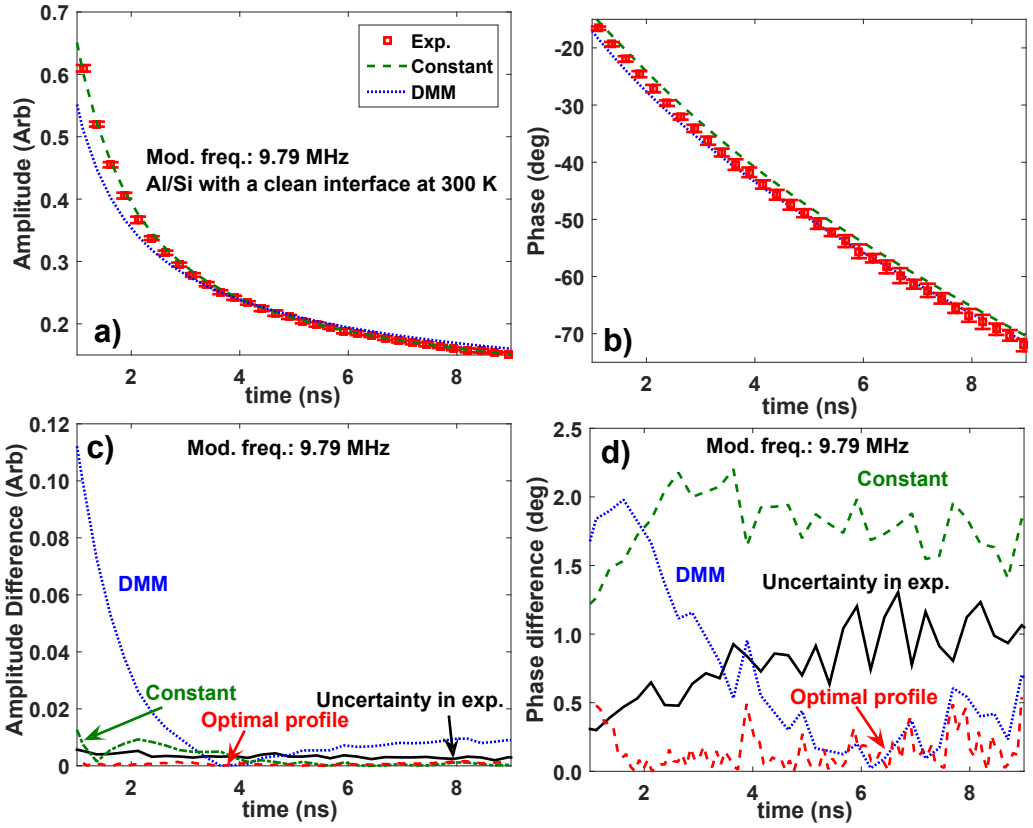

Figure 5.9: Experimental TDTR data (symbols) on Al/Si with a clean interface at 300 K for modulation frequency $f = 9.79$ MHz along with the (a) amplitude and (b) phase compared to the data from the BTE simulations using constant $T_{Si \to Al}$ (dash-dotted lines) and DMM (dotted lines). (c) Amplitude and (d) phase difference between averaged experimental data and the BTE simulations using constant $T_{Si \to Al}$ (dash-dotted lines), DMM (dotted lines), and the optimal profile in Fig. 2 of the main text (dashed lines). The solid line indicates the uncertainty in experiments.

measured value for the clean interface is 280 ± 10 MW/m^2-K.

Here, we demonstrate that neither of the models can explain the experimental TDTR data. As shown in Figs. 5.8 & 5.9, the use of a constant transmission coefficient in the BTE model overpredicts the phase values. Similarly, the DMM underpredicts both the amplitude and phase at the early time of the signals. In Figs. 5.8(c) & (d) and 5.9(c) & (d), we show the deviation in amplitude and phase between the averaged experimental data at a given modulation frequency and the BTE simulations using a constant profile and DMM, demonstrating that the deviation is far beyond the uncertainty in experimental data. The uncertainty is computed by calculating the standard deviation of both amplitude and phase data for multiple runs and multiple locations on a sample.

From these plots, it is clear that neither of the models is capable of explaining the data, and it is also clear that TDTR data depends on the spectral profile of the transmission coefficients. As can be seen in Fig. 5.5, the coefficients we obtain by solving the inverse problem described in Section 5.4 clearly give a superior fit to the measured data for all modulation frequencies for which measurements were performed.

A better comparison for our measurements is with atomistic calculations that are not subject to the highly restrictive assumptions of the AMM and DMM. Performing this comparison, we observe that our measurements agree with numerous molecular dynamics and atomistic Green's function calculations, essentially all of which predict a decreasing transmission coefficient with increasing phonon frequency.(*154–157*) In particular, our measurement of near-unity transmission for phonons with frequencies less than approximately 4 THz is consistent with atomistic calculations on acoustically-matched materials.(*155*, *177*) Our result also agrees with the experimental studies of polycrystalline silicon by Wang *et al*,(*62*) which suggested that

transmission coefficient should decrease with increasing frequency. Our work is thus able to provide unambiguous experimental confirmation of these prior computational and experimental works for the first time while clearly showing that the coefficients predicted by simple models are qualitatively incorrect.

5.7 Interfacial heat flux

Using this transmission coefficient profile, we plot the spectral interfacial heat flux versus phonon frequency and accumulative heat flux versus phonon wavelength in Figs. 5.10. Our results show that most of interfacial heat flux is carried by phonons with frequencies less than 4 THz, with the contribution from higher frequencies strongly reduced due to their small transmission coefficients. In fact, we find that the contribution of phonons with frequencies less than 4 THz is essential to explain our observations: we are unable to explain the measured data without the contribution of phonons with frequencies less than 4 THz. Similarly, we find that we can only explain the measurements using the exact phonon dispersion for Al computed from DFT; simple dispersion relations such as Debye model cannot explain the data because they underestimate the contribution of low frequency phonons to thermal transport.

5.8 Robustness of the measured transmission coefficients

To confirm the robustness of the measured transmission coefficients, we conducted several additional experiments. First, since the energy transmission at the interfaces is considered elastic, the transmission coefficients in theory should be independent of temperature. We performed TDTR measurements on the same Al/Si sample at several temperatures higher than 300 K and compared the experimental results with the calculations using the same transmission coefficient profile measured at 300 K. As shown in Figs. 5.11, the calculation is in excellent agreement with experimental data at 400 K using exactly the same transmission coefficient profile obtained at 300

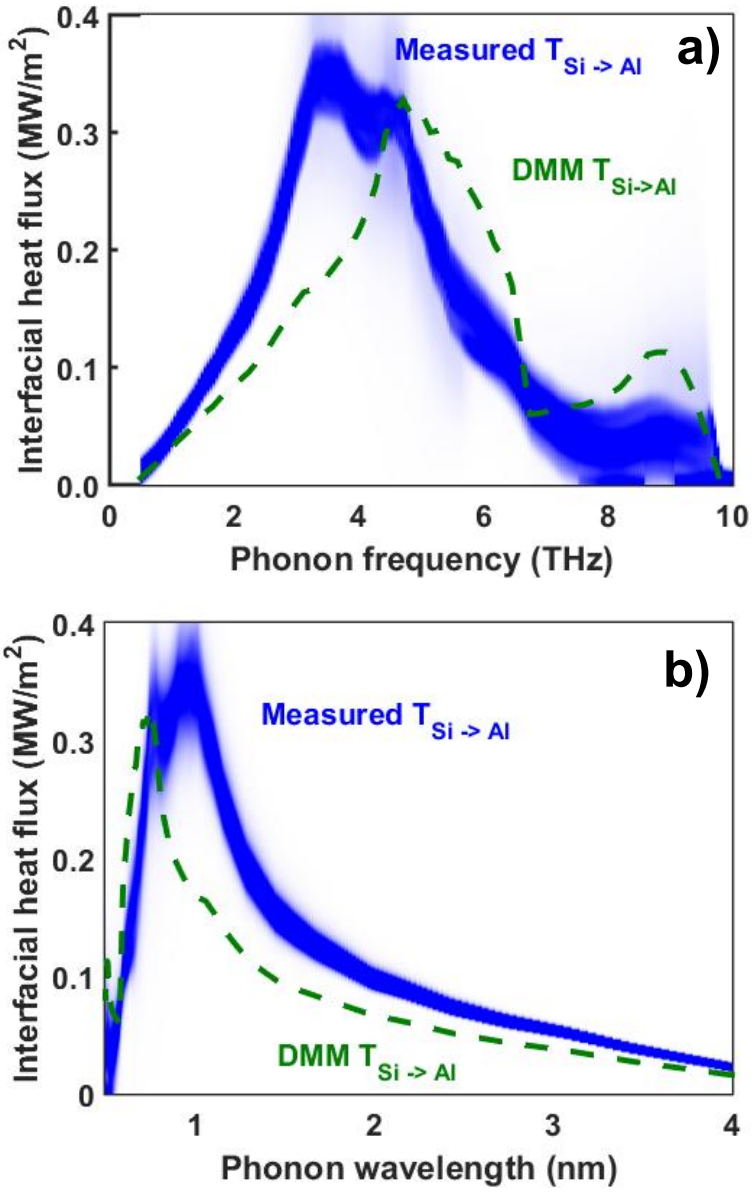

Figure 5.10: Spectral heat flux with the measured (blue shaded region) and DMM (green dashed line) transmission coefficient profiles across the interface versus (a) phonon frequency and (b) phonon wavelength. Phonons with frequencies less than approximately 4 THz carry a significant amount of heat across the interface. The intensity of the shaded region reflects the likelihood of the corresponding transmission coefficients.

K. Note that this comparison does not require any adjustable parameters. Additional measurements at various temperatures are given in the Supplementary Information, and all give excellent agreement.

Second, we measured the transmission coefficients for Al on SiGe. While this material has an additional point defect scattering mechanism compared to pure Si, we expect the transmission coefficients to be nearly the same given that the host lattice is unchanged. The details about point defect scattering in SiGe are given in Appendix D.5. Fig. 5.12 plots the amplitude and phase of the surface temperature decays at different modulation frequencies, demonstrating that the same transmission coefficient profile shown in Fig. 5.6(a) yields a signal that agrees well with this independent data set, again without any adjustable parameters. This result confirms that the measured transmission coefficients for Si and SiGe substrates are indeed the same.

5.9 Effects of atomic structures

We next seek to determine how the atomic structure of the interface affects the spectral content of the phonons carrying heat across the interface. We conducted additional measurements for Al on Si with a native oxide layer (thickness $\sim$ 1 nm as shown in a TEM image in Fig. 5.13(a)) and Si with thermally grown oxide layer (thickness $\sim$ 3.5 nm as shown in a TEM image in Fig. 5.13(b)). Since the oxide layers are sufficiently thin to neglect their thermal capacitance and we only care about the net transmission across the thin layer, we can treat them as part of the interface(*178*) that modifies the transmission coefficient profile.

By solving the inverse problem with the measurement as in Figs. 5.14 & 5.15 as input, we are able to find the transmission coefficient profiles for these two cases as shown in Figs. 5.16. Compared to a clean interface, the transmission coefficients for Al on Si with a native oxide are reduced for most of the phonon modes, except those

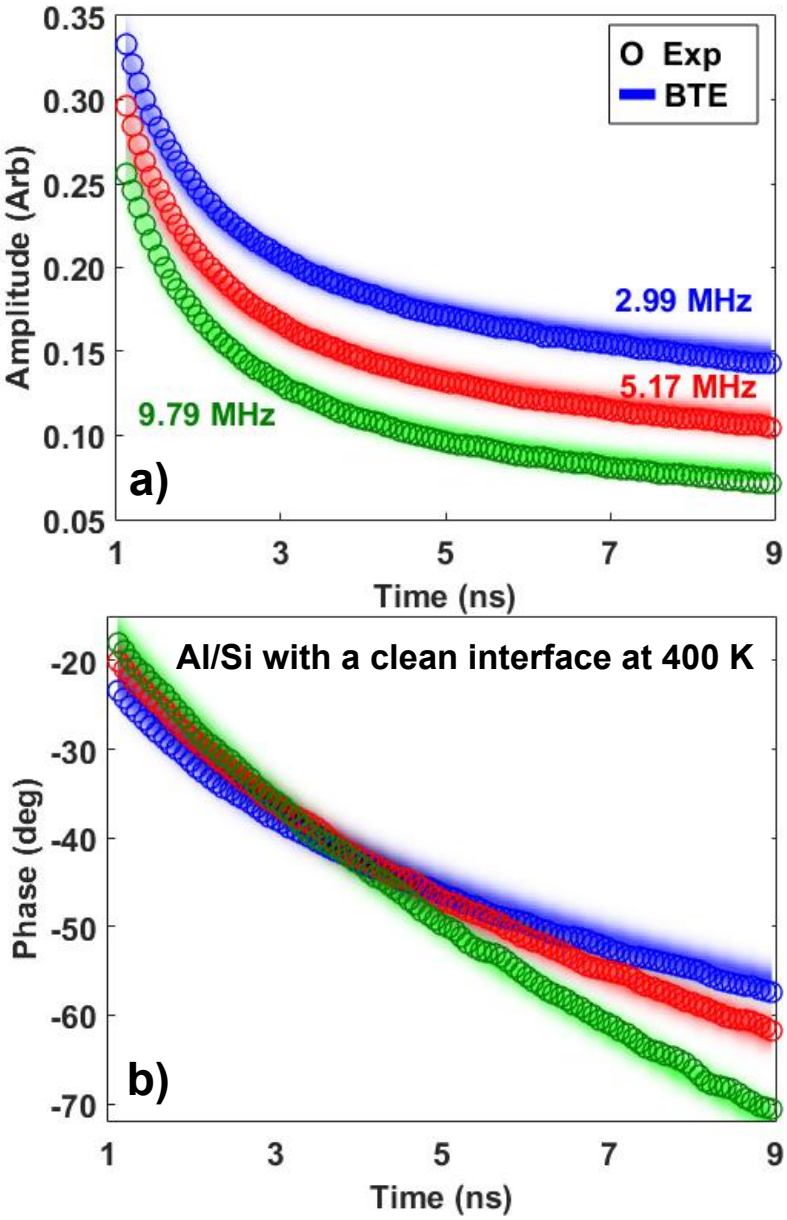

Figure 5.11: (a) Amplitude and (b) phase as a function of time at modulation frequencies $f = 2.99$, 5.17 and 9.79 MHz from experiments (symbols) and simulations (shaded regions) for Al on Si with a clean interface at 400 K. The magnitude and trend of the experimental data are reproduced using the same transmission coefficient profile as in Fig. 5.6 without any adjustable parameters.

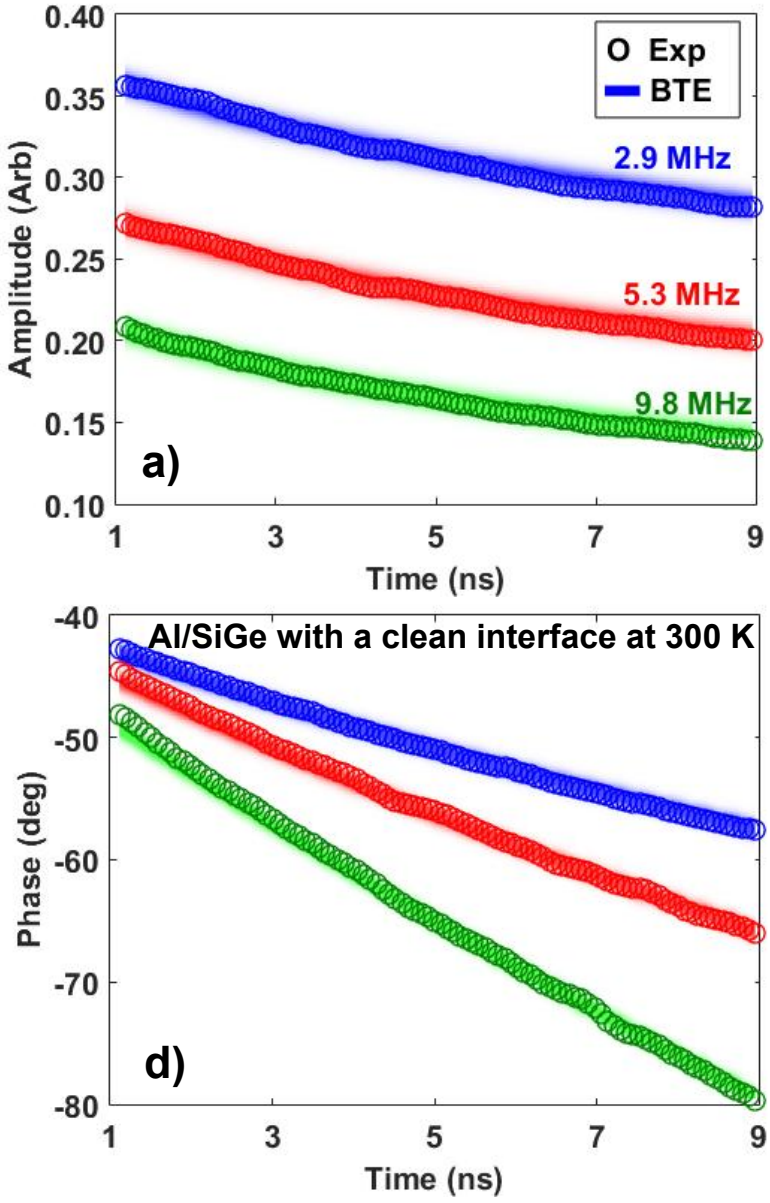

Figure 5.12: (a) Amplitude and (b) phase as a function of time at modulation frequencies $f = 2.9$, 5.3 and 9.8 MHz from experiments (symbols) and simulations (shaded regions) for Al on SiGe with a clean interface at 300 K. The magnitude and trend of the experimental data are reproduced using the same transmission coefficient profile as in Fig. 5.6 without any adjustable parameters.

with long wavelength longer than 1 nm. When the roughness of the interface increases with a thicker oxide layer, the transmission coefficient keeps decreasing and more phonons, especially those with wavelengths between 1 and 3 nm, are reflected at the interface. Therefore, our measurements show that phonons with wavelength shorter than the interface roughness are more likely to be reflected by the interface than phonons with wavelength longer than the interface roughness, and as the interface gets rougher, a larger fraction of the phonon spectrum is affected by the interface. In contrast to prior approaches that measure only interface conductance, here we are able to precisely and unambiguously identify which phonons are more likely to be reflected due to atomic-scale changes in the interface structure for the first time.

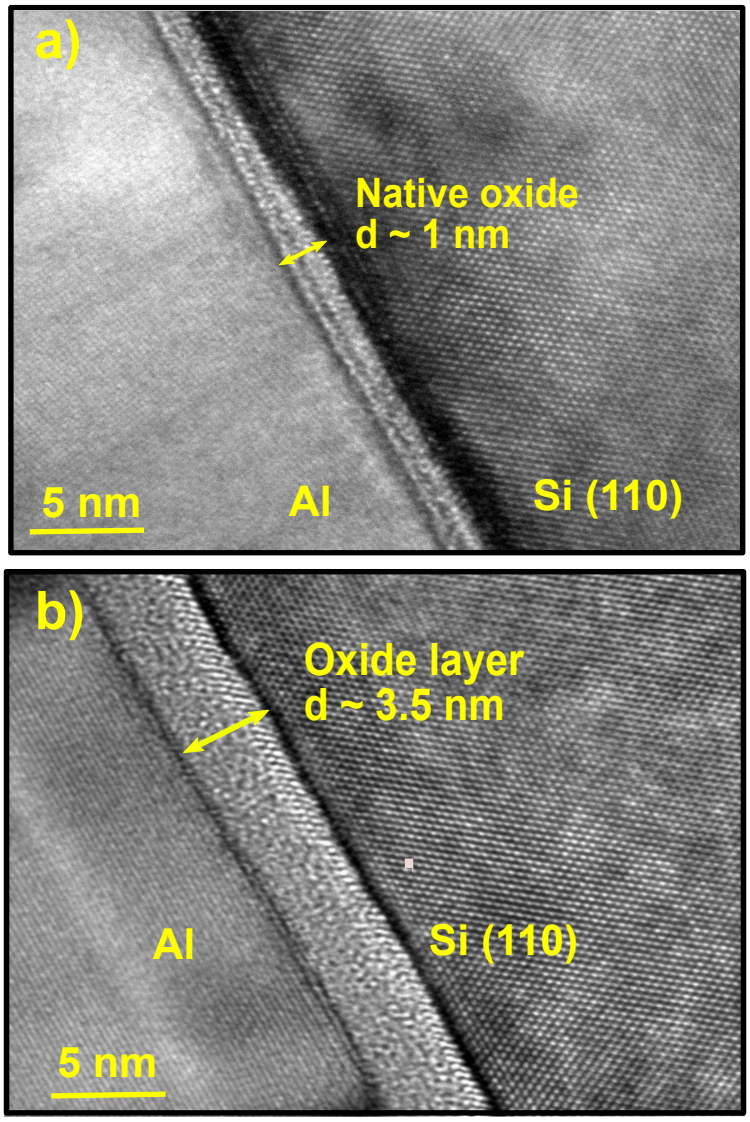

Figure 5.13: TEM images showing the Al/Si sample with (a) native oxide layer (thickness ~ 1 nm) and (b) thermally grown oxide layer (thickness ~ 3.5 nm).

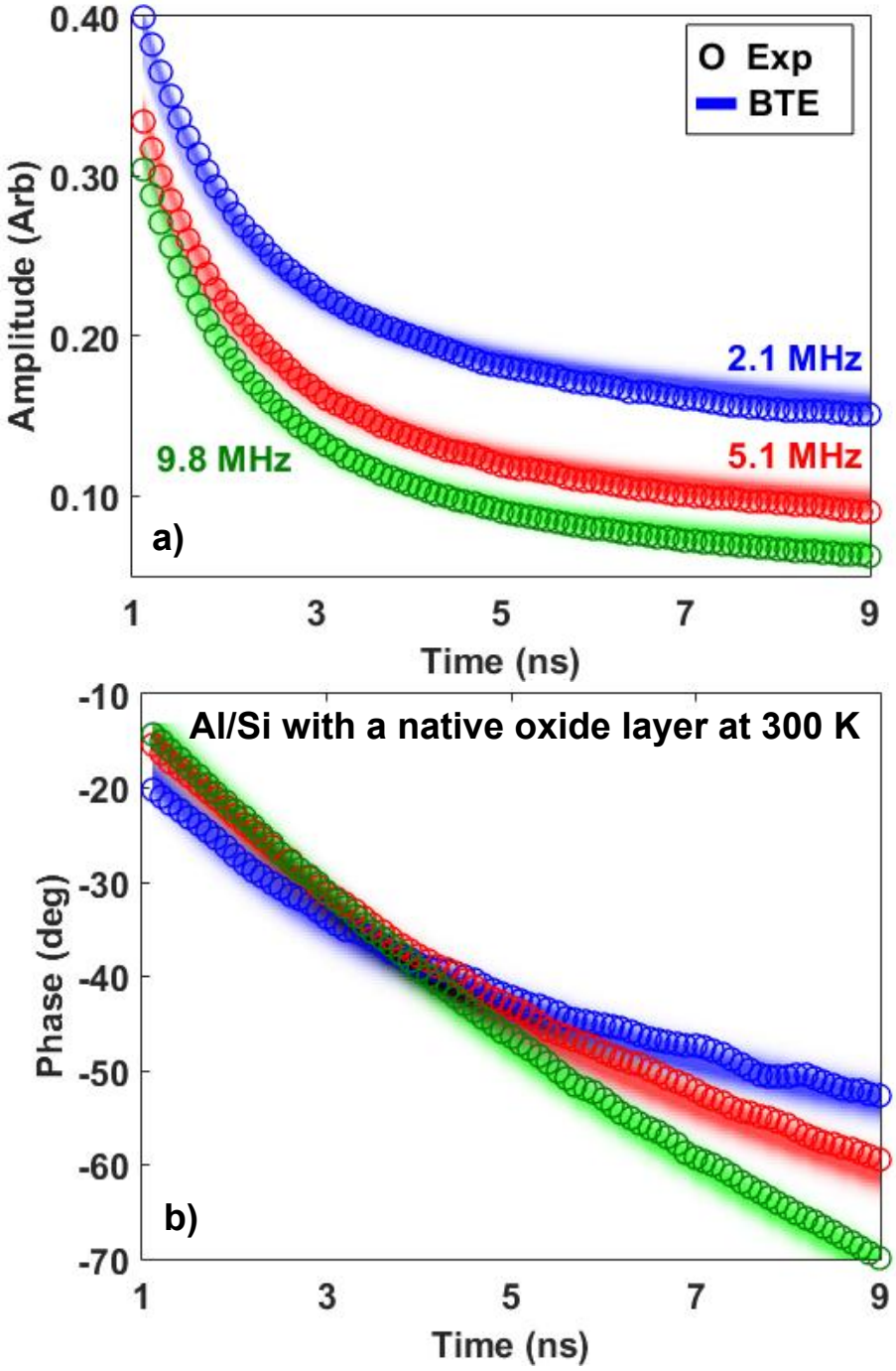

Figure 5.14: (a) Amplitude and (b) phase of the surface temperature decay curves at modulation frequencies f = 1.43, 5.10, and 9.80 MHz of experiments (symbols) and simulations (shaded regions) for Al on Si with native oxide layer.

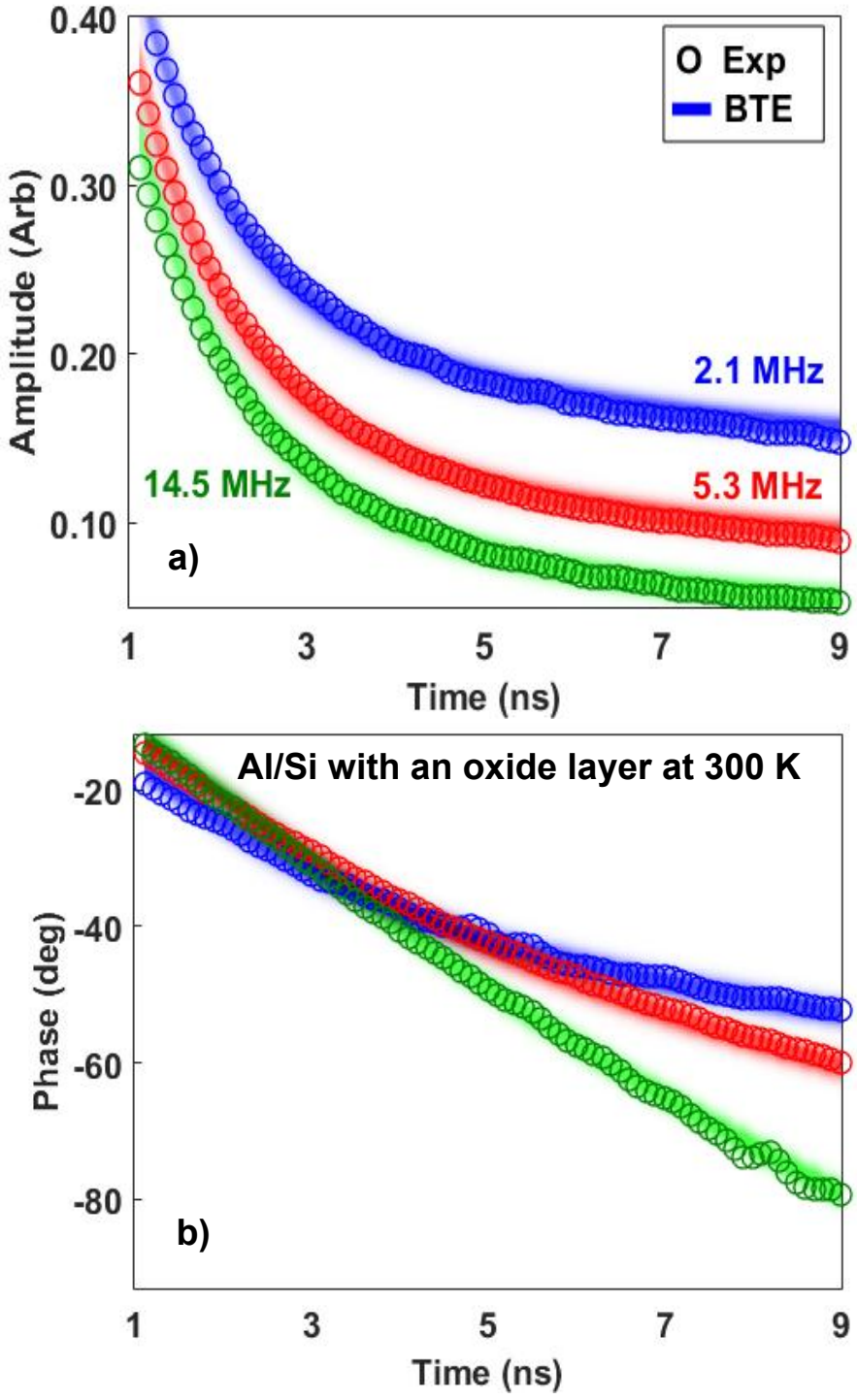

Figure 5.15: (a) Amplitude and (b) phase of the surface temperature decay curves at modulation frequencies f = 1.43, 5.10, and 9.80 MHz of experiments (symbols) and simulations (shaded regions) for Al on Si with a thermally grown oxide layer.

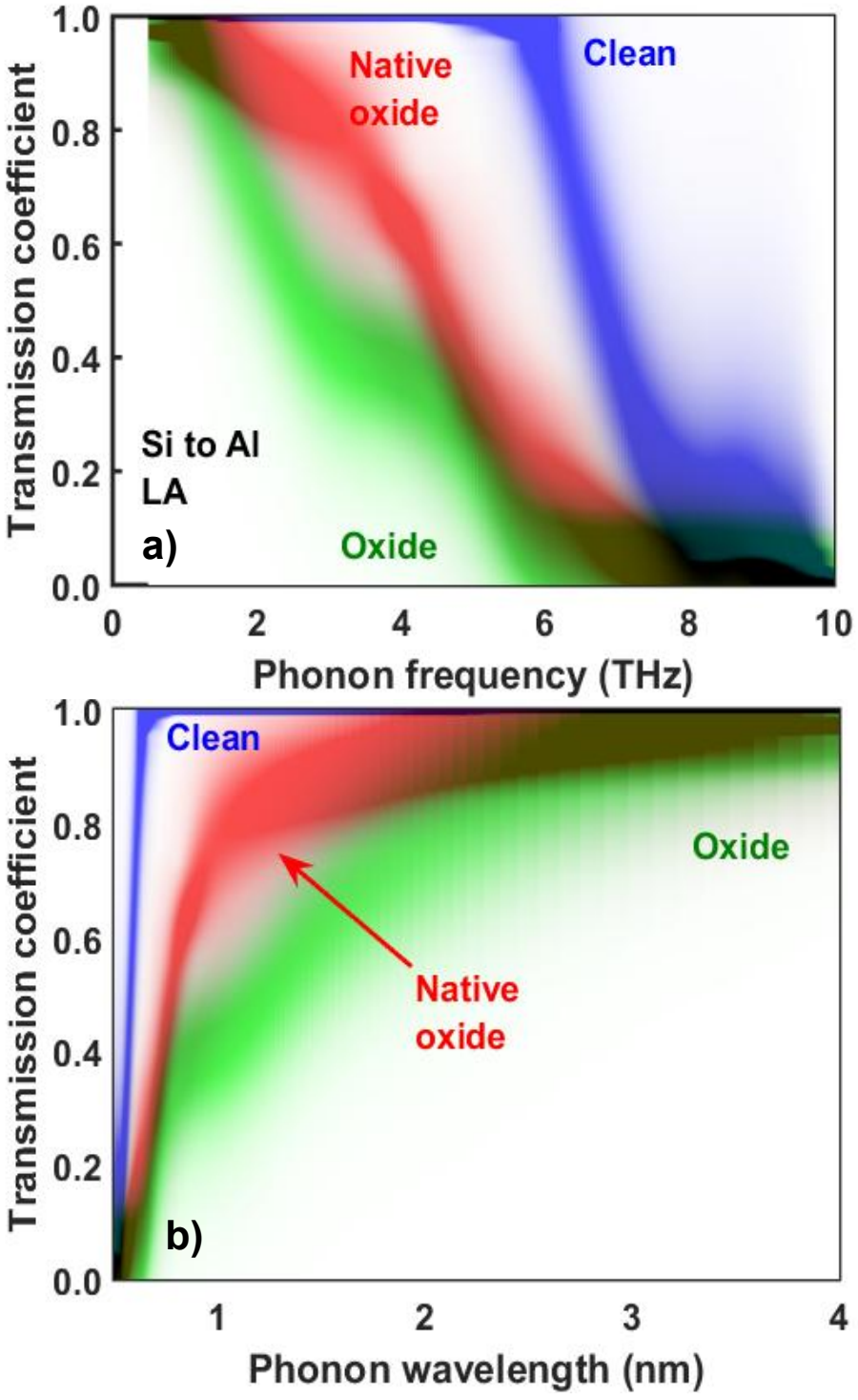

Figure 5.16: Transmission coefficient profiles versus (a) phonon frequency and (b) phonon wavelength for longitudinal modes from Si to Al with a clean interface, with a native oxide layer and with a thermally grown oxide layer. As the interface gets rougher, phonons with frequencies less than 6 THz are more likely to be reflected.

5.10 Role of electrons

The response of a metal to an intense, ultrashort laser pulse is a complex event involving physics that span transport regimes from femtoseconds to microseconds and longer. Initially, photons are absorbed over the duration of the laser pulse by a subset of free electrons in the metal. The hot electrons then interact with the lattice through scattering events.(*179*) To determine the contribution to energy transport from the electrons in Al thin film, we perform the simulations based on a two-temperature model that is able to account for the effects of electrons. Briefly, the two temperature model uses spectral phonon BTE described in Sec. 5.3 coupled with a heat diffusion equation that describes the temperature evolution of the electrons in the Al thin films after absorption of an optical femtosecond laser pulse. The coupled equations are given as following:

$$C_{el}\frac{\partial T_{el}}{\partial t} = \frac{\partial}{\partial x}\left(k_{el}\frac{\partial T_{el}}{\partial x}\right) - g(T_{el} - T_{ph}) \tag{5.32}$$

$$\frac{\partial g_\omega}{\partial t} + \mu v_\omega \frac{\partial_\omega}{\partial x} = -\frac{g_\omega + f_0(T_0) - f_0(T_{ph})}{\tau_\omega} + g(T_{el} - T_{ph}) + \frac{Q_\omega(x,t)}{4\pi}, \tag{5.33}$$

where T_{el} and T_{ph} are the temperatures of the electrons and phonons, respectively, and C_{el} and k_{el} are the volumetric heat capacity and the thermal conductivity of the electrons in Al, respectively. The phonon temperature is linearly coupled to the electron temperature through the electron-phonon coupling coefficient g. The values of all the constants in Eq. 5.32 are tabulated in Table D.1. This system of the equations is solved by a standard finite difference method in a two layered geometry.

We compare the surface temperature responses to a heat impulse with and without the effects of electrons. As shown in Fig. 5.17, due to strong electron-phonon coupling, electrons only affect the heat conduction shortly after the absorption of a heat pulse. After the first 100 ps, the heat conduction is dominated by the phonons. Since a typical signal in a TDTR experiment is usually measured after 500 ps, whether

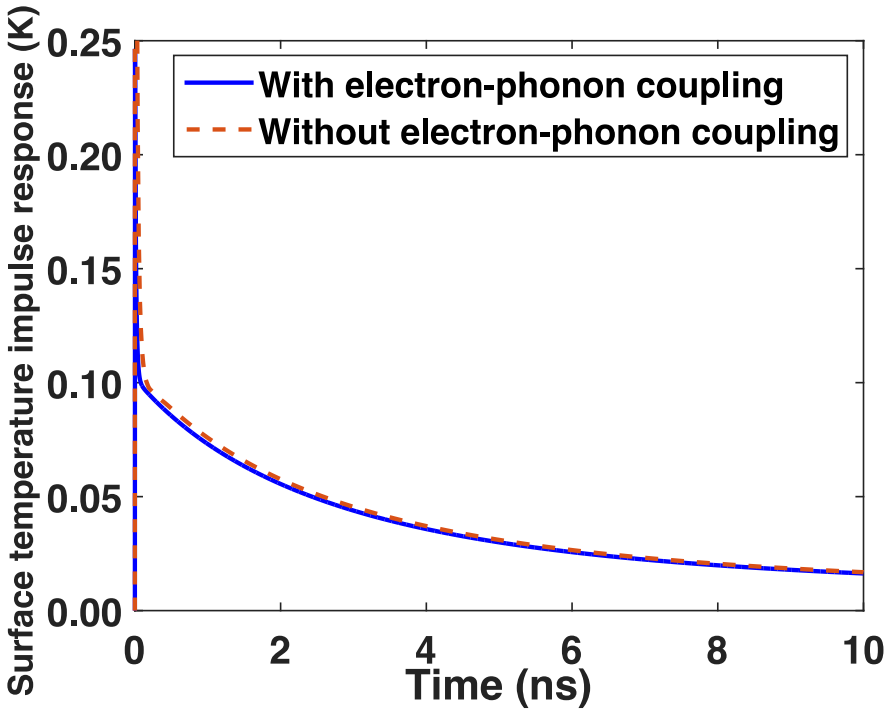

Figure 5.17: The surface temperature decay subject to an surface impulse heating for Al on Si with (solid blue line) and without (dashed red line) the effects of electrons. After 100 ps, the heat is dominated by phonons and there is little contribution from the electrons. Therefore, the electrons have negligible effects on the signal on the timescale relevant to the heat conduction across interfaces.

heat is attributed to phonons or electrons in the metal has a negligible effect on the signal on the timescales that is interested in the experiments. Therefore, our neglect of electrons has no effect on our transmission coefficient measurement.

5.11 Effects of mode conversion

When phonons cross an interface they can change their frequency, in an inelastic process, or polarization, known as mode conversion, which can influence thermal interface conductance.(*180*) In our work, we do not consider inelastic scattering. We justify the neglect of inelastic scattering through the work of prior numerical studies, which have provide evidence that the phonon transmission between two

slightly dissimilar crystalline solids is elastic.(*181*) Considering the phonon frequencies between Al and Si are very similar, there is no evidence that inelastic processes should play a role in the interfacial transport for Al/Si interfaces.

We have carefully examined the effect of mode conversion on our conclusions by rigorously including this process in our BTE model. To examine whether conversion between polarizations would affect the phonon transport across the interface, we conducted our BTE simulation assuming modes maintain their polarization after crossing the interface, or allowing them to change to any polarization while keeping the total transmission coefficient the same. Keeping the total transmission coefficient for a given polarization. Keeping $\sum_j T_{12}^{ij}(\omega)$ invariant, we randomly partitioned $\sum_j T_{12}^{ij}(\omega)$, $\sum_j R_{12}^{ij}(\omega)$ and $\sum_j R_{21}^{ij}(\omega)$ into two different combinations of $T_{12}^{ij}(\omega)$, $R_{12}^{ij}(\omega)$ and $R_{21}^{ij}(\omega)$;in other words, randomly between all the polarizations on the opposite side of the interface. In Fig. 5.18, we show that the surface temperature decay with and without conversion between polarization are essentially identical. Moreover, the spectral interfacial heat flux is also identical with and without conversion. Therefore, we conclude that mode conversion does not have an observable effect on the signal.

The reason that our measurement is not sensitive to mode conversion is that the polarizations in Si do not have extremely dissimilar mean free paths. As our measurement approach relies on the lack of scattering of some modes near the interface, the only way the mode conversion could affect our measurements would be if one polarization consistently changed to another polarization after transmitting through the interface with a drastically different mean free path than the original polarization. Our calculations clearly show that the difference in mean free paths between the polarizations is not sufficient to affect our calculations and hence have any effect on our conclusions.

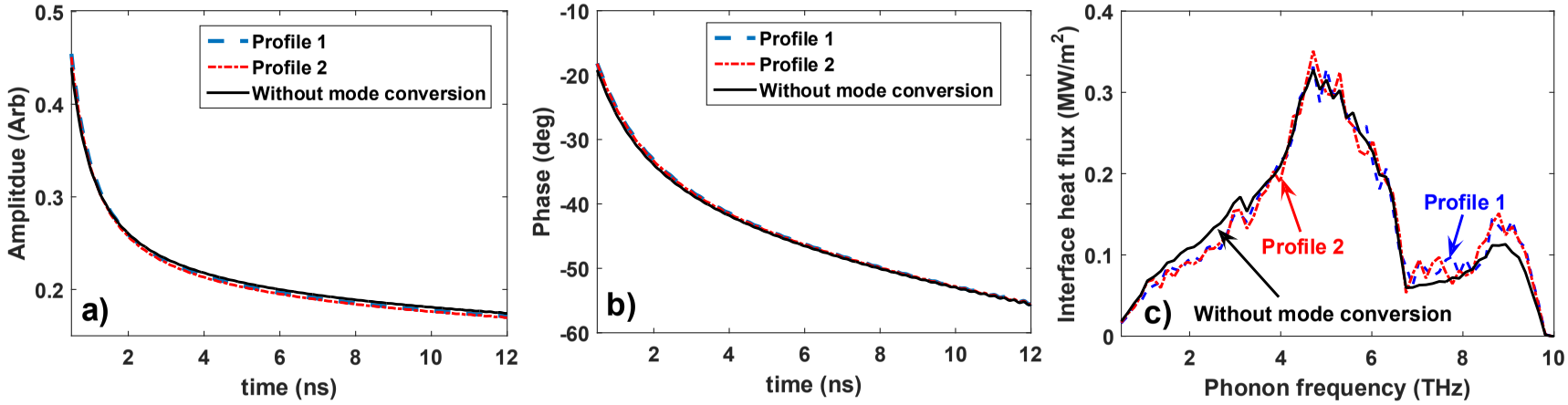

Figure 5.18: TDTR surface temperature decay curves along with (a) amplitude and (c) phase using different transmission coefficient profiles with two completely random partitions of transmitting modes to different polarizations (dashed and dash-dotted lines) and without mode conversion (solid line; assuming phonons maintain their polarization as they cross the interface). (c) Spectral interfacial heat flux versus phonon frequency predicted using different transmission coefficient profiles with mode conversion (dashed and dash-dotted lines) and without mode conversion. Mode conversion does not have an effect on the signal and conclusions beyond the uncertainties already considered in our model.

5.12 Discussion

Our work has considerable implications for thermal metrology and technological applications. First, we have shown that TDTR is capable of providing considerable microscopic detail about thermal phonons if the measurements can be properly interpreted using a microscopic transfer function with ab-initio input. Unlike with the macroscopic transfer function, our approach provides quantitative details on the spectral content of the heat carried by phonons in the sample. As a corollary, using the macroscopic transfer function to interpret TDTR data on certain samples can lead to erroneous results. For example, the apparently correct measurement of silicon thermal conductivity appears to be a fortuitous cancellation of two factors: the high transmission coefficient of low frequency phonons leads to an increased contribution to heat flux that offsets the deviation from Fourier's law that occurs due to a lack of scattering. If these two factors were not balanced, the apparent thermal conductivity of Si would not coincide with the bulk value. Therefore, the conventional TDTR interpretation does not necessarily provide the actual physical properties of the materials.

Second, our measurements show that the spectral profile of transmission coefficients is essential to understanding thermal transport across interfaces. Due to a lack of knowledge about interfaces, the phonon transmission coefficients are often predicted with a variety of simple models. However, this work shows that none of these models are capable of explaining the experimental measurements. Therefore, including an accurate spectral transmission coefficient profile is essential to properly describing thermal phonon transport across interfaces.

Third, our work provides strong evidence that elastic transmission of phonons across an interface is the dominant energy transmission mechanism for materials with similar phonon frequencies. Our microscopic transfer function does not incorporate electrons or inelastic scattering yet is able to explain all of the measurements we

performed. We conclude that inelastic transmission and coupling between electrons in metals and phonons in semiconductors have little influence on the energy transport for the materials considered here.

Fourth, our results demonstrate that disorder at interfaces plays an important role in the spectral content of the heat transmitted through the interface and provides strategies to alter interface conductance. For instance, in applications like LEDs where the heat dissipation rate across interfaces is to be enhanced, the key to increasing interface conductance is to minimize the reflection of high frequency phonons (with wavelength shorter than the surface roughness of the interface) by reducing defects; low frequency phonons (with wavelength longer than the surface roughness of the interface) are likely to be mostly transmitted already. On the other hand, the strong frequency dependence of the transmission coefficients can be exploited to create thermal phonon filters to selectively remove parts of phonon spectrum, analogous to optical long-pass filters. Phonons with wavelength much longer than the characteristic roughness of an interface are more likely transmitted through the interface while short-wavelength phonons are mostly reflected. The thermal phonon spectrum responsible for heat conduction can thus be manipulated by controlling the atomistic roughness of an interface.

Finally, our work exemplifies the powerful insights into heat conduction at the atomic scale that can be obtained through the interwoven application of experimental measurements in the quasiballistic heat conduction regime, ab-initio phonon transport modeling, and electron microscopy. Through our approach, we are able to directly link the atomic structure of an interface to the spectral content of heat crossing it for the first time. Such a capability will permit the rational understanding and control of interfacial heat transport at the atomic level, a capability that is expected to impact numerous application.